

The magnetic Bp star 36 Lyncis

II. A spectroscopic analysis of its co-rotating disk

M.A. Smith¹, G.A. Wade², D.A. Bohlender³, C.T. Bolton⁴

¹ Department of Physics, Catholic University of America, Washington, DC 20064, USA; Present address: Space Telescope Science Institute, 3700 San Martin Dr., Baltimore, MD 21218 Email: msmith@stsci.edu

² Department of Physics, Royal Military College of Canada, Kingston, Ontario, Canada K7K 4B4

³ National Research Council of Canada, Herzberg Institute of Astrophysics, 5071 W. Saanich Rd., Victoria, BC Canada V9E 2E7

⁴ David Dunlap Observatory, University of Toronto, P.O. Box 360, Richmond Hill, ON, Canada, L4C 4Y6

Received ??; accepted ??

Abstract. We report on the physical properties of the disk-like structure of B8 IIIp star 36 Lyncis from line syntheses of phase-resolved, high resolution spectra obtained from the *International Ultraviolet Explorer* archives and from newly obtained ground-based spectra of the H α absorption profile. This disk is highly inclined to the rotational axis and betrays its existence every half rotation cycle as one of two opposing sectors pass in front of the star. Although the disk absorption spectrum is at least ten times too weak to be visible in optical iron lines during these occultations, its properties can be readily examined in a large number of UV “iron curtain” lines because of their higher opacities. The UV Fe II and Fe III lines in particular permit a determination of the disk temperature: $7,500 \pm 500$ K and a column density of $3^{+3}_{-1.5} \times 10^{20}$ cm $^{-2}$. The analysis of the variations of the UV resonance lines brings out some interesting details about the radiative properties of the disks: (1) they are optically thick in the C IV and Si IV doublets, (2) the range of excitation of the UV resonance lines is larger at the primary occultation ($\phi = 0.00$) than at the secondary one, and (3) the **relative strengths of the absorption peaks** for the two occultations varies substantially from line to line. We have modeled the absorptions of the UV C IV resonance and H α absorptions by means of a simulated disk with opaque and translucent components. Our simulations suggest that a gap separates the star and the inner edge of the disk. The disk extends radially out to ≥ 10 R $_{\star}$. The disk scale height perpendicular to the plane is ≈ 1 R $_{\star}$. However, the sector causing the primary occultation is about four times thicker than the opposite sector. The C IV scattering region extends to a larger height than the H α region does, probably because it results from shock heating far from the cooler disk plane.

Key words. stars: individual: 36 Lyncis – stars: chemically peculiar – stars: magnetic fields – stars: circumstellar matter – ultraviolet: stars – X-rays: stars

1. Introduction

In a companion to this paper, Wade et al. (2006; hereafter Paper 1) have redetermined the magnetic and rotational periods and surface abundances of the He-weak B8p star 36 Lyncis (HD 79158). Using data from the *International Ultraviolet Explorer* (IUE) satellite, Shore & Brown (1990; hereafter SB90) discovered the presence of circumstellar plasma through the periodic modulations of the strengths of its C IV and Si IV resonance lines. Following the model of Shore (1987), SB90 found that these modulations are due to a disk-like structure surrounding the star.¹

¹ The term “disk” will be used in this paper to describe circumstellar matter corotating in or near the magnetic equatorial plane of the star. Evidence is accumulating that the gas density of these structures is unevenly distributed in azimuth

According to this picture, the wind from the magnetic poles flows out along open field lines to infinity, much as for unmagnetized stars. However, at lower magnetic latitudes the wind behavior and geometry is complex. Since the wind particles from this zone are charged, they cannot easily cross the magnetic loops, and the high velocity flow is effectively quenched. At intermediate latitudes, the flow is constrained to follow closed magnetic loops. As they cross the magnetic equator, the particles collide and shock with streams originating from the other hemisphere, generating EUV or X-ray emission in a large, spheroidal post-

in this plane. The structure may have a discrete inner edge, may be decentered, may be nonisothermal around the disk **at a given radius from the star’s center**, and may be warped out of coplanarity (see e.g., Townsend & Owocki 2005; hereafter TO05).

shock region (e.g., Babel 1997, Babel & Montmerle 1997 (hereafter BM97), Babel & North 1997). Post-shock particles cool and settle toward the equatorial plane. Steady state is achieved as particles return to the star's surface or escape through the disk's outer edge. In this picture a cool disk co-rotates with the star and resembles a wobbling inner tube. As fixed external observers, we see "shell" absorption components in the UV resonance and H α lines near the rest frame at those times during the rotation cycle when a section of the disk **transits** the star. In spectra of hot Bp stars a slightly redshifted emission is observed in the UV lines when the disk is viewed "face on."

Since the pioneering studies of Babel and collaborators, several important advances have been made in the hydrodynamic modeling of Bp disks. The first of these was the inclusion of the feedback effects of the wind particle weight on the magnetic field loops (ud-Doula & Owocki 2002, uO02). This weight causes the loops to sag, thereby permitting disk particles to fall back to the star at low magnetic latitudes. This process leaves an effectively gas free region close to the star. In addition, for sufficiently high ratios of magnetic to wind energy density η , circulation of wind efflux proceeds on a timescale of a few days and, in certain η regimes, chaotically. These models suggest that the effective coverage factor of the star by the disk can be large, even occulting the entire star for near edge-on viewing angles. Models that include radiative cooling of the wind/disk shock interface (Tonnesen et al. 2002) indicate that the hot zone is mainly confined to the outer region of the disk yet also extends out of the equatorial plane. Recent theoretical work (e.g., Preuss et al. 2004, TO05) suggests that matter can accumulate on low potential energy surfaces, well outside the disk plane.

A large number of studies have shown that many and perhaps all Bp stars with measurable dipolar fields harbor co-rotating magnetospheres. Periodic ultraviolet variations have also been found in a few β Cep stars (Henrichs et al. 1998, Floquet et al. 2002, Neiner et al. 2003), in the O7V star θ^1 Ori C (Walborn & Nichols 1994, Stahl et al. 1996), and in He-weak stars as late as type B8 (Shore & Brown 1990b, Shore et al. 2004). To generalize, the periodic variability of the CIV and/or N V lines is a hallmark of Bp stars with oblique dipolar magnetic fields (Smith & Groote, hereafter SG01).

36 Lyn is one such star. It lies near the cool edge of the He-weak Bp domain and shows prominent CIV and N IV line variations. In order to take advantage of the available H α observations and *IUE* archival data, the improved determination of its rotational and magnetic geometry, and of our improved understanding of the theoretical properties of disks, we have modeled the variations of several UV and optical lines in this star's disk. From our results we are able to provide quantitative estimates of its thermodynamic and geometrical properties.

In their analysis of disk properties of four Bp and β Cep stars, SG01 utilized archival spectra from the *International Ultraviolet Explorer* satellite to analyze the time variations of UV ultraviolet resonance lines and the

"iron curtain" background of weak lines populating the far-UV spectrum. For this study we were able to include new phased H α absorptions, as taken from Paper 1; see the journal of observations in this paper for details. The finer **sampling** in phase and the higher quality of these observations over the *IUE* data provide additional constraints on the properties of the circumstellar material.

The UV data for these programs are extant high-dispersion *IUE* echellograms obtained through the large-aperture and of the Short Wavelength Prime (SWP) camera. These data were obtained from the MAST archives.² and constitute a total of 26 spectra (a 27th spectrum, SWP 32982, was lost to the *IUE* project; Levay 2003).

| | |
|------------------------------------------------|-------------------------|
| Mass M | $4.0 \pm 0.2 M_{\odot}$ |
| Radius R | $3.4 \pm 0.7 R_{\odot}$ |
| Effective temperature T_{eff} | $13,300 \pm 300$ K |
| Surface gravity $\log g$ | $3.7 - 4.2$ |
| Period P_{rot} | 3.83475 days |
| Projected rotation speed $v_{\text{e}} \sin i$ | 48 ± 3 km s $^{-1}$ |
| Inclination i | $56 - 90^{\circ}$ |
| Dipole strength B_{d} | 3210-3930 G |
| Phase of mag. equator passage | 0.0 |
| Photospheric abundance [Fe] | +0.8-1.1 dex |

Table 1. Some characteristics of 36 Lyn from Paper 1.

2. Spectral synthesis computations

To perform the analysis of the *IUE* spectra, we utilized a suite of programs written by I. Hubeny and collaborators and LTE solar-abundance atmospheres computed by Kurucz (1993) for input to these programs. The first of these is *SYNSPEC*, which is a photospheric line synthesis program written by Hubeny, Lanz, & Jeffery (1994). For the line synthesis computations using this program, we adopted the metallic abundances tabulated in Paper 1. We also employed the features in *SYNSPEC* that permit the convolution of instrumental and rotational broadenings to the computation of the line profiles. The disk integration algorithm approximates the star as a 500×1000 grid. The spectrum was computed at steps of 0.01Å. We should note that our adaptation of Kurucz model atmospheres with normal **abundances does not** include the effect of enhanced backwarming through the atmosphere due to the overabundances of the Fe group ions. Fortunately, non-LTE effects appear to be small for most UV metallic spectra of B stars with $T_{\text{eff}} < 25,000$ K (e.g., Smith, Sterken, & Fullerton 2005).

Our goal in this analysis will be to assess the effects of an absorbing magnetospheric disk on UV lines in the star's spectrum as the disk moves across and off the star's surface. To simulate the signatures of this structure on the

² Multi-Mission Archive at Space Telescope Science Institute, in contract to NASA.

composite spectrum, we used the radiative transfer program *CIRCUS* (Hubeny & Heap 1996, Hubeny & Lanz 1996) to compute strengths of absorption or emission components of lines in a circumstellar medium from input quantities such as disk temperature, volume density, column density, areal coverage factor (the fraction of the star covered by the disk at maximum occultation phase), and microturbulent velocity. Although *CIRCUS* can accommodate as many as three separate circumstellar “clouds” with as many independent parameter sets, in this paper we assume the disk to be homogeneous. In its solution of the radiative transfer, *CIRCUS* allows the user to compute the line flux with the line source function set either to zero or the Planck function at the local temperature. This feature can be used to compute the disk spectrum in full non-LTE (scattering approximation) or LTE modes, respectively. **We used the scattering approximation for our analysis of UV resonance lines.**

Other key input parameters include the disk volume density and turbulent velocity. The volume density enters only through the ionization of the species, which is mainly determined by the temperature. Our input density 10^{11} cm^{-3} was the order of magnitude determined for hot Bp star disks by SG01. This parameter was used only to set the ionization equilibria for the elements responsible for the resonance lines. However, we note that these equilibria are mainly sensitive to temperature. Except for the absorptions of the SiIV, CIV, and NV resonance lines, the overwhelming majority of the UV metal lines in our computations are optically thin. Since the spectral signatures then depend on the volume of absorbers, a degeneracy arises between two geometrical factors of the disk: its area and column length along the observer’s line of sight. For convenience we have performed our spectral analyses, excluding the occultation models discussed in §5, by assuming that the coverage factor of the disk is unity when it passes in front of the star. Our analysis, given our choice of i and β , will validate this assumption.

The final ingredient of our models is the treatment of line of sight velocities. Because the magnetosphere co-rotates with the star’s surface, no differential velocities exist along the line of sight to the star during occultation (transit). SG01 found that turbulent velocities in the range of $0-20 \text{ km s}^{-1}$ resulted in similar absorptions of ensembles of iron lines. SG01 also found a broadening of the AlIII resonance lines of at least 25 km s^{-1} at occultation phases $\phi = 0.0$ and 0.5 . Based principally on this result, for the analysis of the disk lines, we have adopted an arbitrary value of 20 km s^{-1} , or about twice the local sound speed.

3. Basic picture

3.1. The Goldilocks absorption effect on iron lines

In addition to the modulation of the resonance lines, one of the phenomena that drew our attention to 36 Lyn was the contrasting behavior of its iron lines in the optical and UV

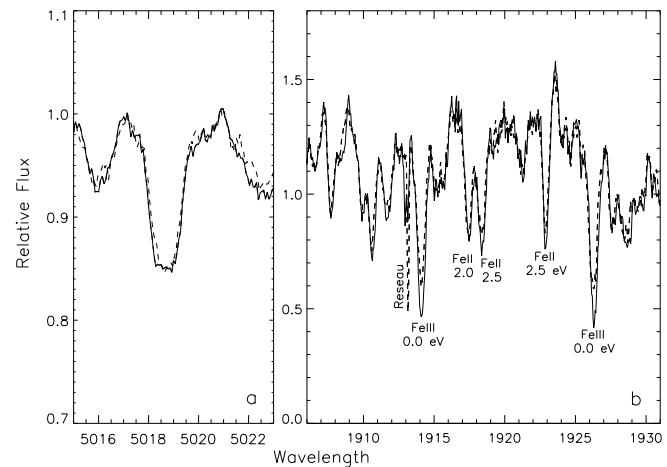


Fig. 1. *Panel a:* A comparison of two observations of the Fe II $\lambda 5018$ line region obtained at during nonoccultation $\phi = 0.90$ (2001 December 02; dashed line) and at the occultation phase, $\phi = 0.02$ (2000 February 12; solid line). *Panel b:* A comparison of high-resolution *IUE* (unsmoothed) spectra centered on a wavelength region that contains a mixture of strong Fe II and Fe III lines. **The fluxes in a and b are relative, or are given in c.g.s. units multiplied by 10^{10} , respectively.** The dashed line spectra represent the photospheric spectrum while the solid line depicts the spectrum at occultation phases.

spectral regions. The two panels of Figure 1 show the different behaviors of strong optical Fe II and UV Fe III lines during occultation and nonoccultation phases. In Fig. 1a the line core of the Fe II $\lambda 5018$ at the occultation phase $\phi = 0.97$ (solid line) is no deeper than during the nonoccultation phase, $\phi = 0.82$. It is possible that weak bumps occur on the latter profile. These are likely to be signatures of an inhomogenous surface distribution of Fe on the star’s surface, as found in Paper 1. In contrast to the optical lines, Fig. 1b shows that several low-excitation Fe II and Fe III lines in the $\lambda 1900$ region deepen significantly during occultation phase. This is again consistent with the strengthenings of low-excitation lines during disk occultation of the hot stars studied by SG01. The strongly contrasting different behaviors of the optical and UV lines (the former responds to surface inhomogeneities and the latter to circumstellar conditions) may seem surprising at first. However, they can be understood after computing the opacity spectra for physical conditions we will find in the disk. Taking $T_{disk} = 7,500 \text{ K}$ and microturbulence $\xi = 20 \text{ km s}^{-1}$, we find that the Fe II $\lambda 4923$ and $\lambda 5018$ lines in this disk medium have opacities of about $4 \times 10^{-23} \text{ cm}^{-2} \text{ atom}^{-1}$. By comparison, the opacities of the UV iron lines depicted in Fig. 1b are typically $50 \times$ higher than this value. These values fall in a region of parameter space for which the disk absorptions of optical lines are practically invisible. In contrast, the optical depths of the UV lines are near unity, and thus they respond rather sensitively to changes in column length. Because

we are in a window for which the opacities are just right, we call this a “Goldilocks” absorption effect. Thus, for Bp stars with higher effective temperatures, we might expect various surface and disk conditions to cause competing effects on the optical and UV metallic line profiles. Abundance patches along the magnetic equator will cause high-excitation lines (those usually visible at optical wavelengths) to strengthen as these regions cross the observer’s meridian, whereas low-excitation lines would strengthen at disk occultation phases. The result could be confusing for a panchromatic abundance analysis if the presence of a disk were not taken into account. For stars cooler than 36 Lyn winds will be very weak, and we expect surface inhomogeneities due to diffusion to dominate all the lines.

4. Spectral Analysis of Line Absorption

Our analysis of the disk properties begins by examining the ionization of iron atoms in the disk, first by comparing specific strong lines in the spectrum and then by assessing their group effects in differential spectrophotometry.

4.1. Disk diagnostics from lines of iron and low-ionization atoms

4.1.1. Analysis of individual lines

The ionization equilibrium of iron shifts quickly from Fe^{1+} to Fe^{2+} in the temperature range 7,000 K–8,000 K. One can exploit this sensitivity by comparing the increases of Fe II and Fe III lines during occultation. A sample of these lines is shown in Fig 1b. We have computed *CIRCUS* models to simulate these strengthenings in detail in order to determine both a mean temperature and column density of the disk. By matching the *ratio* of Fe II to Fe III strengthenings during occultation phase, we found that the temperature is tightly constrained to values of $7,500 \pm 500$ K. Our internal errors in this determination have been doubled in order to take into account any potential effects of non-LTE on iron line formation. The same models, but now fitting to the *mean* increase in iron-line strengthenings, led to a less secure estimate of the column density, $3^{+3}_{-1.5} \times 10^{20}$ cm $^{-2}$. We estimate the error on this parameter to be a factor of three, based on uncertainties in disk coverage factor, the assumed high Fe abundance of the disk, microturbulence, and our oversimplification of the homogeneity of the disk. For low stages of ionization, the ionization potentials of aluminum are similar to iron. This fact encouraged us also to model the variations of other resonance lines of this element, such as Al II $\lambda 1670$, and Al III $\lambda 1855$, $\lambda 1863$. As before, we exploited the rapid ionization shift from Al $^{1+}$ to Al $^{2+}$ in the temperature range 7,000–8,000 K. Again, we found a best fit with $7,500 \pm 500$ K. The fits to the mean strengthenings of the line during occultation phases led to a column density of 1.5×10^{20} cm $^{-2}$. We estimate a factor of two **for the error in the latter value**. The column density de-

termination from aluminum lines is well within the **error range** found from individual Fe II and Fe III lines.

We have similarly attempted to constrain temperatures from silicon lines arising from neighboring ionization stages, but this has proven difficult. In the case of silicon, only two unblended Si III lines are strong enough to be visible. In addition, the mean strength of several apparent “Si III” lines is overestimated because of close blends with iron lines. These tend to drive the apparent abundance of Si $^{2+}$ well above optically-derived values. The absence of variation in the forbidden Si III resonance line at $\lambda 1892$ (which would otherwise be useful for analysis of extended low-density media) can be used only to rule out a temperature above 9,000 K and/or a column density above 3×10^{21} cm $^{-2}$. The Si III resonance line at $\lambda 1265$ has a broad saturated core. At occultation phase $\phi \approx 0.0$, the core strengthens and broadens. We can duplicate this strengthening only for $\xi > 20$ km s $^{-1}$ in our models. This is true to even a greater extent for the C II $\lambda\lambda 1335$ –6 doublet, which, for a good fit of the line core and strength variations, requires large ξ values of 50 km s $^{-1}$.

4.1.2. Analysis of the “Iron Curtain” lines

Following the methodology of SG01, we used *CIRCUS* and *SYNSPEC* to fit the strengthenings of the absorption lines during disk occultation. This analysis was performed by first summing all fluxes within each echelle order of a *IUE/SWP* spectrum and then computing the mean absorption in this order for all spectra observed at similar phases. The division of occulted by nonocculted phase **spectra**, minus one, gives the fractional absorption in an UV spectrophotometric representation of the observations. This divided low-resolution spectrum can be compared directly with the computed photospheric spectrum divided by the computed spectrum of the star absorbed by the model disk. For the disk spectrum of 36 Lyn, the overwhelming majority of lines are optically thin. This fact introduces a degeneracy between the disk areal coverage (effectively, the disk “height”) and the column density. Since the UV opacity is almost entirely due to Fe-group elements, a second fitting degeneracy occurs between column density and iron abundance. We also note that the value $\xi = 20$ km s $^{-1}$ produces a wavelength-averaged absorption that is 35% higher than the mean absorption produced by $\xi = 10$ km s $^{-1}$. These uncertainties enter heavily into the error budget for the column density given above. Using these parameters, a disk temperature of 7,500 K, and an assumed photospheric value of $T_{\text{eff}} = 13,000$ K, we modeled the UV spectrophotometric data. The comparison of this *CIRCUS* model with the observations is given in Fig. 2a. In Figs. 2b and 2c we exhibit the comparisons for β Cep and σ Ori E, which are taken from SG01.

To give the reader an idea of strengths of “typical” lines in the UV spectrum, we note that for 7,500 K the median cross section for lines with wavelengths above $\lambda 1300$ is 20 times stronger than the underlying hydrogenic opac-

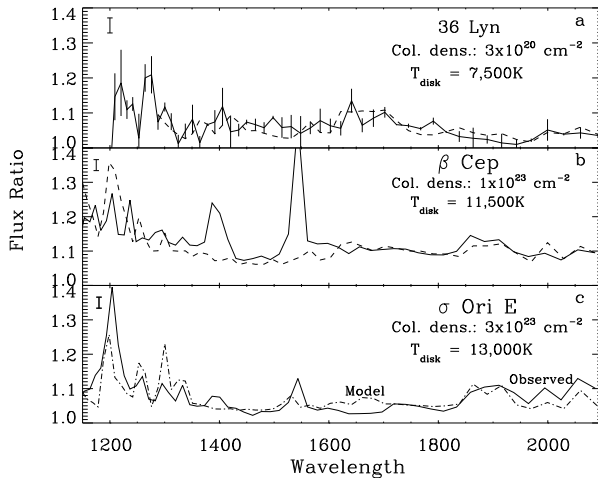


Fig. 2. Observed (solid line) and computed-plus-1.0 (dashed line) ratios of disk Fe-absorption spectra for 36 Lyn, β Cep, and σ Ori E. Spectra for 36 Lyn are the same as those used for Fig. 1. The models indicated assume a full disk occultation of the star and a value $\xi = 20 \text{ km s}^{-1}$. The temperature used in this fit was taken from the fittings discussed in § 4.1.1.

ity ($2 \times 10^{-23} \text{ cm}^{-2}$ per atom). Only 2.5% of lines in the wavelength range $\lambda\lambda 1300\text{--}2100$ are optically thick for our reference column density of $3 \times 10^{20} \text{ cm}^{-2}$. Because of the degeneracy between coverage and column density one can match the mean levels of absorption by increasing the disk column density by factors of 6 and 30 while decreasing its coverage area by factors of 10 and 100, respectively.

Bjorkman, Bjorkman, & Wood (2000) and Smith (2001) have pointed out that for spectra of circumstellar disks around B stars, aggregates of strong lines in selected wavelength intervals provide temperature diagnostics. The character of these aggregates shifts through changes in ionization. For example, a well-known “Fe III bump” appears in the disk temperature range 10,000–16,000 K. This bump is visible in the spectrophotometry of the hot Bp stars analyzed by SG01, but it does not appear in the 36 Lyn data. However, Fig. 2a **reveals a just detectable bump** in the range $\lambda\lambda 1550\text{--}1750$. Inspection of our synthesis results shows that this feature is composed almost entirely of optically thin Fe II lines, consistent with our assumptions. Putting all these facts together, and again using a coverage factor of 100%, an iron abundance of +1.04 dex, $T_{\text{disk}} = 7,500 \text{ K}$, and $\xi = 20 \text{ km s}^{-1}$, our **fitting to the mean absorptions** in Fig. 2a leads to a column density of $3 \times 10^{20} \text{ cm}^{-2}$. We also notice that the column density is at least a factor of 100 lower than those found in disks of the hot Bp stars σ Ori E and β Cep (SG01). According to a preliminary analysis, the column density for the disk of another B8p star, HD 21699, is probably even lower, suggesting that the disk column tends to increase monotonically with effective temperature among magnetic Bp stars. Yet, there is no trend in disk parameters with the stars’ field strengths.

The agreement of the disk temperatures inferred from individual Fe and Al lines on one hand and the spectrophotometric curtain absorptions on the other **hand** is important in justifying our geometric results below that the inner region of the disk is largely evacuated. Recent radiative equilibrium models of circumstellar disks of Be stars assume a slow outward flow of matter such that the density decreases outward with radius. These models predict a local **temperature** minimum in this disk component. For 36 Lyn this temperature should be $\sim 6,000 \text{ K}$. However, our models indicate a strengthening of many Fe II lines that is not observed. This fact argues against the presence of a substantial contribution from a low temperature component to the disk.

4.2. Ultraviolet resonance lines

4.2.1. Basic Characteristics of the resonance doublets

To determine the characteristics of the C IV, Si IV, and N V spectra, we first plotted these lines’ equivalent widths with respect to rotation phase. This was accomplished by using the phase zero point and period given in Table 1. We used these to form **two average spectra: one taken near mid-occultation phase and the other near the quadratures when the disk is seen face-on**. The two resulting spectra were taken from *IUE* observations SWP 27038, 27052, 27070, 27091, 31996, 32014-5, 32947, 32971-2 and SWP 32024, 32057, 32990, respectively. Figure 3 compares these spectra for the C IV and N IV doublets. The bottom of this figure gives a sense of the statistical variations through the r.m.s. spectra for these lines from the available data. Detailed modeling of the resonance lines in both the photospheric (actually “disk face-on”) and disk-absorbed spectra with *SYNSPEC* shows that the C IV and Si IV lines suffer blends.

Figure 4 exhibits examples of the computed and observed template spectra of the C IV doublet at quadrature and mid-occultation phases. We have offset the disk-absorbed spectra downward for clarity. As this figure shows, the photospheric spectra can be modeled well using the solar C and the Fe-rich abundances specified in Paper 1. The disk-absorbed spectra of C IV can also be well modeled, with one stipulation, using a disk temperature $T_{\text{disk}} = 25,000 \text{ K}$ and the column density given in §4.1.1. **We stipulate that our residual** mismatches probably result from our use of a disk microturbulence, 20 km s^{-1} , that is probably much less than the turbulence in at least some regions of the disk. Subsequent trials showed that values of at least 50 km s^{-1} are required. High turbulence values (if it is a true microturbulence) were also noted by SG01 and were also reported for the our modeling of 36 Lyn’s C II doublet profiles in §4.1.1. The mismatches can be seen in the broad core of the $\lambda 1548$ line in Fig. 4 (lower solid line). The mismatch is not so noticeable in the $\lambda 1550$ feature because it is a semi-resolved blend of the C IV $\lambda 1550$ component and Fe II $\lambda 1550.3$; the added turbulence is not as large as the 0.5 \AA separation between

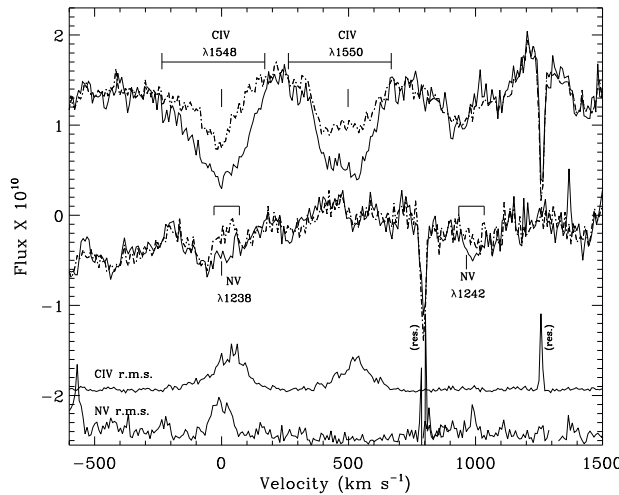


Fig. 3. Maximum (solid line) and minimum (dot dashed line) absorption spectra for the CIV and NV lines in 36 Lyn (upper plots) and their renormalized difference r.m.s. spectra of all spectra (lower plots). The spectra represented are those in Figs. 1b and 2c. The velocity reference is zero for the rest frames of the $\lambda 1548$ and $\lambda 1238$ components of the CIV and NV doublets, respectively. Instrumental “reseaux” are indicated.

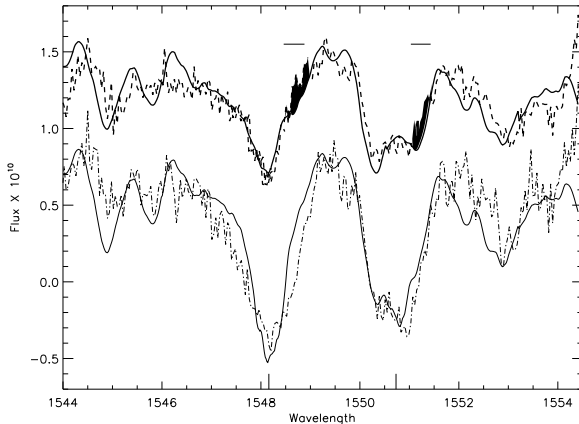


Fig. 4. The observed maximum (dot-dashed line) and minimum (thick dashed line) absorption spectra for the CIV lines in 36 Lyn. Corresponding spectra computed for the photosphere and during disk occultation (solid lines) are shown. The maximum and disk-absorbed spectra are shifted -0.7 units for clarity. The dark shading, interpreted as emission, is the difference between the minimum absorption and photospheric profiles.

the two $\lambda 1550$ lines. Another interesting mismatch is the series of low-excitation Fe II lines in the regions $\lambda\lambda 1544$ –6 and $\lambda\lambda 1552$ –3 for the disk-absorbed spectrum. Our simulations suggest that a higher microturbulence would ameliorate these mismatches. However, these high turbulences, for which we have so far no physical explanation, are not otherwise important to this analysis.

The measured equivalent width differences of the C IV $\lambda 1548$ and $\lambda 1550$ components are 550 mÅ and 440 mÅ, respectively. The corresponding maximum and minimum equivalent widths of the Si IV $\lambda 1394$ and $\lambda 1403$ lines are 173 mÅ and 155 mÅ, and for the N V doublet 65 mÅ and 40 mÅ, respectively. The C IV and Si IV doublet ratios are close to unity. Therefore, we conclude that these lines are optically thick.

The small shaded regions in Fig. 4 are possible emissions due to the disk in the plane of the sky. These can be expected to contribute line-scattered flux in the line of sight to observer at this phase. The emissions measured from the face-on (observed) minus computed (photosphere only) spectrum are -31 mÅ and -15 mÅ, which corresponds to 5% ($\pm 5\%$), of the total difference. Given the errors on these quantities, they should not be overinterpreted. However, we may safely say that any emission contributed by the disk in these lines is small or negligible.

4.2.2. Temperature and column density results for the resonance lines

Our modeling of the equivalent widths of the resonance lines is most sensitive to the estimated temperature and column density. Therefore, other arguments must be used to constrain these values. For a sample derived from absorptions of just a few lines, a temperature solution is generally poorly constrained, and so the argument is frequently made that the most likely temperature is that which results in maximum absorption (or emission), or equivalently, minimum column density. Moreover, the optical thickness requirement on the C IV and Si IV absorptions can be used to constrain the region of temperature and density space. In Table 2 we present disk temperatures and column densities required to fit the absorption equivalent widths measured for the stronger component of the N V, C IV, Si IV and Si III resonance doublets. The column densities displayed for the emission cases in the table are somewhat arbitrary and are intended to show τ scales for the lines. In these computations we have utilized photospheric abundances and coverage factors of unity. Because we do not have foreknowledge of the line excitation temperatures in the disk, we computed the strengths both in emission and absorption for a range of temperatures and evaluated them to determine temperature limits. We also searched for “optimal” values of the emission/absorption temperatures. Optimal temperatures are those for which lines are formed most efficiently and thus require minimum column densities per unit τ . Lower and upper temperature limits were likewise evaluated by assuming that the gas responsible for absorptions might have column densities as large as $\sim 10^{19}$ cm $^{-2}$. This is equivalent to a few percent of the column lengths derived in §4.1. Even if this assumed column value were too low, the ionization fractions at these limits drop off quickly with temperature. Thus, a smaller fraction would produce little change in our temperature ranges. The values given in the “emis-

| N V ($\lambda 1238$) | T_{disk} | Col. Dens. (Abs.) | τ_{line} | T_{disk} | Col Dens. (Emis.) | τ_{line} |
|---------------------------|------------|----------------------|---------------|---------------|----------------------|---------------|
| T_{max} | 53,000 | 1.5×10^{19} | .001 | 69,000 | 6×10^{17} | .001 |
| T_{mid} | 43,000 | 1×10^{18} | .05 | 50,000 | 5×10^{13} | .005 |
| T_{min} | 33,000* | 1×10^{10} | .03 | 30,000* | 6×10^{17} | .02 |
| C IV ($\lambda 1548$) | T_{disk} | Col. Dens. (Abs.) | τ_{line} | T_{disk} | Col Dens. (Emis.) | τ_{line} |
| T_{max} | 30,000 | 5×10^{19} | 0.3 | 50,000 | 2×10^{17} | 0.03 |
| T_{mid} | 28,000 | 1×10^{18} | 3 | 30,000 | 1×10^{14} | 0.003 |
| T_{mid} | | | | 25,000 | 2×10^{16} | 0.03 |
| T_{min} | 25,000* | 4×10^{19} | 12 | 20,000* | 6×10^{17} | 3 |
| Si IV ($\lambda 1394$) | T_{disk} | Col. Dens. (Abs.) | τ_{line} | (No emission) | | |
| T_{max} | 30,000 | 7×10^{18} | .004 | | | |
| T_{mid} | 20,000 | 1×10^{14} | .01 | | | |
| T_{min} | 15,000* | 4×10^{17} | 4 | | | |
| Si III ($\lambda 1206$) | T_{disk} | Col. Dens. (Abs.) | τ_{line} | (No emission) | | |
| T_{max} | 20,000 | 1×10^{18} | .03 | | | |
| T_{mid} | 15,000 | 1×10^{18} | 1 | | | |
| T_{min} | 10,000* | 1×10^{19} | 22 | | | |

Table 2. Derived disk temperatures (K), column densities (cm^{-2}), and τ_{line} for model fits for UV resonance lines.

sion” columns of Table 2 were obtained by assuming that, as for CIV in the previous section, they are equal to $\approx 5\%$ of the range of the equivalent width variation. From the computed line cross sections determined in these calculations, we find that the *emission* column densities are low enough for the lines to be optically thin, contrary to their optical thickness when observed at occultation.

One may appeal to the formation process of the “super ions” to narrow the temperature ranges still further from those given in Table 2 because the resonance lines are produced by an isotropic process, namely scattering. Then because the line photon addition or removal is caused by the same disk ions (seen from different viewing angles at these phases), one expects the column density determined for the two cases to be roughly the same. This expectation is not met in the CIV and NV column densities given in Table 2. In fact, the best absorption column values are at least an order of magnitude higher than for the emissions. This fact suggests that one of the two temperature limits, and not the optimal one, offers the best solution. According to the higher optical depths in the CIV lines indicated by the measured doublet ratios, this limit is likely to be the lower one. We suspect it is the lower of the two limits for the NV lines too. This reasoning suggests that the true temperature range derived for these lines is smaller than the values tabulated. Based on these considerations, we represent in Table 2 our estimates of most realistic temperatures by asterisks and italics. In cases where a temperature limit seems to be indicated, we have chosen the lower one.

4.2.3. Variation of the resonance lines with phase

To quantify the behavior of the resonance lines with phase, we have computed line strength indices of 36 Lyn by computing the ratio of fluxes within narrow velocity limits around the line center(s) to the residual fluxes in the net (unrectified) spectra contained in the parent echelle order. This technique is not subject to errors of continuum rectification and placement. The measurement limits were set to $\pm 65 \text{ km s}^{-1}$ from line center, or just beyond the rotational limits on the profile. A comparison of indices extracted from both these broader and narrower limits for CIV showed that they followed the same form, but the broader limits decreased the apparent errors.

Figure 5 depicts the line strength indices with phase for CIV, **Si IV**, and NV. The curves exhibit a narrow primary peak centered near $\phi = 0.00$, which for 36 Lyn corresponds to the rotation of the South magnetic pole onto the receding limb of the star and an underresolved “secondary” peak occurring near 0.55 cycles.

Note in Fig. 5 that the relative CIV absorption peaks have nearly the same heights. However, for Si IV the second peak is stronger, while it is much weaker for NV, as indeed we find it is also for H α (§5.3) and the less excited ions of Si III, Al III, and Fe III (not shown). The differing ratios suggest that the range of ionization temperatures of gas within the sector causing the first occultation is narrower than for the secondary occultation sector. **MacFarlane, Cohen, & Wang (1994)** have pointed out that models of photoexcitation of ions by soft X-rays predict a broad distribution of excited ions. This does not seem to occur in the primary occultation segment, suggesting that this segment (and probably the secondary one as well) is excited by collisions and not photoionizations.

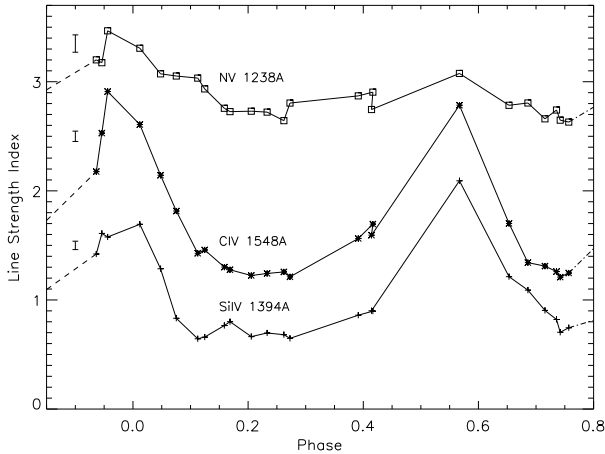


Fig. 5. Line strength indices of the NV $\lambda 1238$, CIV $\lambda 1548$, and SiIV $\lambda 1394$ lines for 36 Lyn with magnetic/rotation phase. The curves have been offset for clarity.

5. The line strength-phase curves of the resonance and H α lines

5.1. The models

The morphologies of the line strength-phase curves, such as those shown in Fig. 5 and the H α curve shown in Fig. 4 of Paper 1, offer the possibility of determining geometrical properties of the disks of Bp stars. Although the disk column density is relatively low, the ratio of the absorptions of the resonance doublet members indicates that these features are optically thick. This means that the absorption process can be recast by merely computing the occulted area of the star. We wrote a program to compute this absorption by considering a cylindrical opaque ring or disk with origin coinciding with the star's center. Its tilt with respect to the rotational equator is fixed by the magnetic obliquity β . In our formulation all light from the star is occulted by this structure. Physically this means that the source function relative to the background stellar photospheric emissivity is negligible. This could mean, for example, that the radiative transfer in the lines is dominated by resonance scattering. However, it is also possible that a similar absorption profile can result if the line is formed in LTE. The key requirement in either case is that the emergent flux from the slab with changing viewing angle remains constant during the occultation event.

In our construct the magnetic and rotational obliquities may be set to arbitrary values. We adopted the values $i = \beta = 90^\circ$, which are consistent with the limits found in Paper 1. Thus, our basic model of the “disk” reduces to an opaque cylindrical ring oriented perpendicular to the star's rotational axis. As the star rotates, one or the other of the disk segments rotates in front of the star, except at quadrature phases 0.25 and 0.75 when the magnetic poles cross the center of the disk. The free parameters of our opaque cylindrical model consist of inner and outer

disk radii, given by r_i and r_o , and a disk semiheight h , out of the equatorial plane, all of which are expressed in units of R_* . Because the circumstellar disk is assumed to be axisymmetric and centered at the center of the star, one need only integrate over half the star's area. We used a star disk grid of 2000×1000 pixels and integrated the data over 1° phase intervals. Because of the appearance of an ingress feature discussed below, we eventually modified our program to approximate the effects of an optically thin extension out of the magnetic and disk plane. In this second class of models, the extension was approximated by a translucent absorption that falls off from an initial value of $1/e$ at the edge of the opaque component. This absorption is parameterized by a second scale height h_S . This component is layered over/under the opaque components, making it extend further out from the plane.

A weakness of our formulation is interpretational: one does not know where along the line of sight the absorption occurs at a given viewing angle. Despite this limitation, our approach offers the advantage of not tying the results artificially to a completely opaque disk geometry. A secondary, minor weakness in our picture is that the H α opacity appears not to be infinite ($\tau \sim 5$ in our CIRCUS models).

Before we start the geometrical analysis, we ask what limits apply to the extent of the radial disk. We can estimate this extent by computing the Alfvén radius R_A , which is the radius at which the magnetic and wind energy densities are equal. This is given by the simple relation:

$$R_A = \eta^{\frac{1}{4}}, \quad (1)$$

where η , or the ratio of magnetic to wind energy densities (uO02), is given by:

$$\eta_* = B_*^2 R_*^2 / (\dot{M} v_\infty). \quad (2)$$

Here B is the mean surface field, R_* the stellar radius, \dot{M} the mass loss rate, and v_∞ is the terminal wind velocity. From Paper 1, we take $B = 3$ kG and $R_* = 3.4 R_\odot$. BM97 considered a range of mass loss values $10^{-10} - 10^{-11} M_\odot \text{ yr}^{-1}$ for the active X-ray star IQ Aur ($T_{eff} = 13,000 - 16,000$ K). 36 Lyn is undetected in the X-ray regime, so we will assume $\dot{M} = 10^{-11} M_\odot \text{ yr}^{-1}$. Effects of the wind are not detectable on the resonance lines, so we will assume an arbitrary value $v_\infty = 600 \text{ km s}^{-1}$ (BM97 assumed 800 km s^{-1}). These values lead to a value $\eta \approx 10^7$. Then, an application of equation (1) yields $R_A \approx 50 R_*$. Although these simple relations may or may not scale precisely in a high η regime, we can still be assured that the Alfvén radius for 36 Lyn is very large. We will be at liberty to consider disk radii of a few tens of stellar radii.

5.2. Fitting of UV resonance line variations with phase

The line strength curves of the resonance lines of 36 Lyn shown in Fig. 5 have three general features: (1) a peak with central maximum near $\phi = 0.0$, (2) a quick drop-off to a narrow core (a half-width half-maximum of 0.06

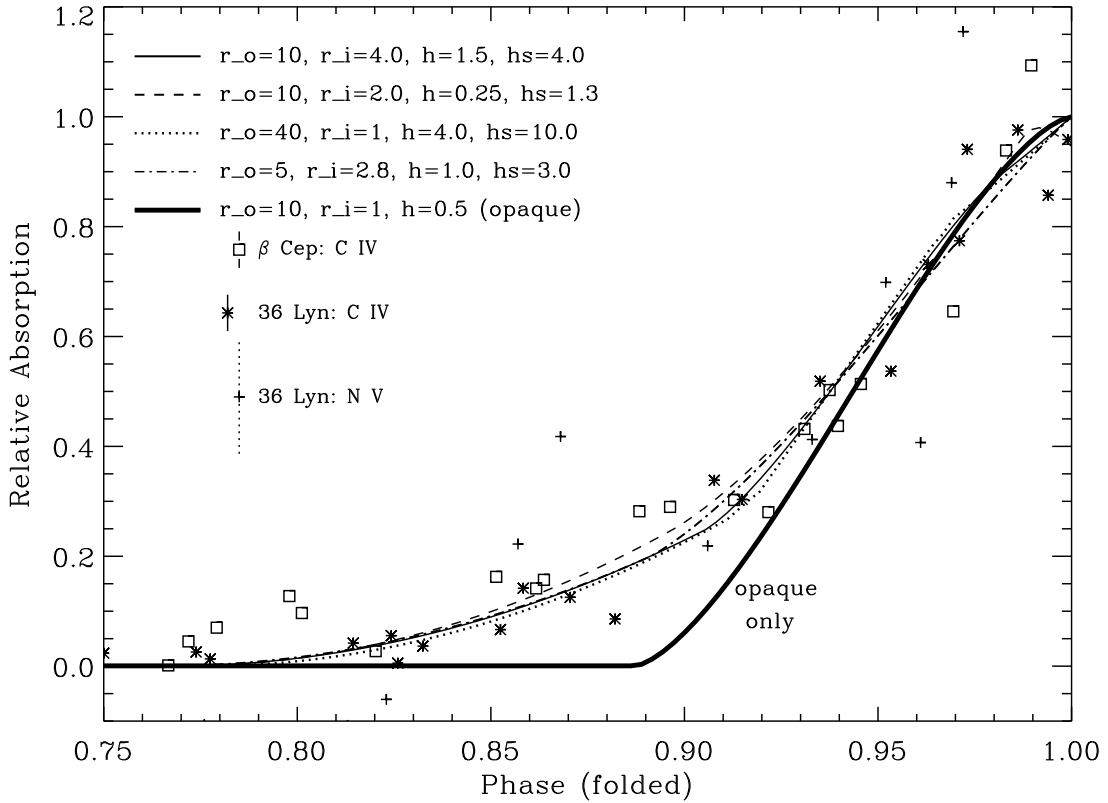


Fig. 6. Fits to excess absorption with phase of the C IV and N V resonance lines of 36 Lyn and C IV lines of β Cep at primary occultation. The data are taken from Fig. 5 and SG01, respectively, and folded around $\phi = 1.0$ (disk viewed edge-on). Error bars are indicated on the data symbol annotations. The various coded lines are fits from the two-component model and, where indicated, single opaque component model for the disk absorption ($r_o = 10R_*$, $r_i = 1R_*$, $h = 0.5R_*$). For convenience all fits indicated were computed for the simple geometrical case of the star viewed equator-on and with a magnetic inclination of 90° .

cycles), and (3) a tapered ingress/egress “tail” extending from phase **1.00** to ≈ 0.82 and 0.18 (**1.18**). To study these curves further, we folded the C IV and NV equivalent widths measured around the occultation midpoint phases. For reference, we did the same for the C IV data of β Cep. For both stars the estimated phase of maximum absorption is not exactly at 0.00. In the interest of coaligning the peaks of the two stars and **comparing the morphologies**, we shifted the phases slightly to remove this difference. The Fig. 5 data manipulated in this fashion are shown in Figure 6, along with five model fits.

After a search throughout our model parameter space, we found that it is impossible to fit all features with a opaque-disk model **and** a small height h . The essence of the problem is that all such models produce an “*M*”-like feature centered at $\phi = 0.0$ or 0.55 in the equivalent width-phase curve. This minimum occurs because the **absorption** from the disk is greater just before/after the central conjunction. At the former times the disk appears canted to an external observer, and hence, like Saturn’s rings often viewed from Earth, has a relatively large projected area. Conversely, for opaque disk models with large values

of h the absorption reaches a flat plateau well before central occultation. The absence of either a pointed or *M*-like absorption profile maximum in Fig. 6 drives our modeled disk semiheight h to intermediate values of 0.5 – $1R_*$. Our best models suggested a clean break between the inner edge of the disk and the star.

The disk parameters have different degrees of influence on various portions of the phase curve. The shape of the peak (*M*-like, triangular, or a flat plateau) is largely determined by the disk height. The narrowness/broadness of the core component of the absorption profile is determined by the arctangent of the disk’s semiheight h and its outer radius r_o . Thus, these two parameters are coupled. A uniform disk connected to the star, with $r_i \approx 1R_*$, would cause the absorption to appear soon after the face-on phase, i.e., at $\phi < 0.80$. The general absorption profile would then acquire a triangular shape that is not observed. However, none of these parameters in the opaque model representation can explain the ingress tail in Fig. 6. The failure to match the tail worsens if one departs from the simple $i = 90^\circ$, $\beta = 90^\circ$ geometry. **Reducing the magnetic angle β does not change the shape of the**

curve but deemphasizes the effect of a given separation of the disk from the star, typically by $\sim 30\%$. Observing the star from a smaller i aspect does even more of the same, but more importantly it triangularizes the profile such that there is no turn over or plateau near the maximum, or tail extension at the minimum (limb contact). Likewise, the neglect of limb darkening deemphasizes any absorption tail. To remedy the deficiencies of the single-component opaque model in Fig. 6, we developed the two-component disk model described above.

As the disk rotates from its face-on orientation in the two-component model, absorption from the disk first is evident as the peripheral translucent component advances over the star's limb, in advance of the opaque edge. The difference in the absorption curves between the one and two-component models is substantial. In Figure 6 we show best fit models for $r_o = 5R_*$, $10R_*$, and $40R_*$. As with the one-component models, we found that fitting the data with large r_o requires that the r_i values be made small until finally the inner edge of the disk reaches the star's surface. However, for extensive disks, e.g. $r_o = 40R_*$, the semiheight of the disk would be nearly $15 R_*$ if the disk reached down to the star. We can be skeptical that this class of large-disk models is realistic for real Bp disks. A second practical consideration is that models producing tolerable fits must have not only large h values but proportionately even larger heights h_S . Just as with the former class of opaque models, one must invoke separate arguments to discard the possible solutions with largest and smallest disk radii. To address whether disks can be much thicker or thinner in h than $1R_*$ will require sophisticated hydrodynamic models that include radiative cooling and the effects of post-shock flows.

Interestingly, our two component models require that the ratio h_S/h be close to 2.5–3, i.e., the value of the exponential constant e itself. This fact tends to validate the basic picture that the CIV absorptions are optically thick and become optically thin at 2.5–3 scale heights. The implied value of $\tau_{\lambda 1548} \sim 10$ in the disk plane is also within only a small factor (perhaps 20%) of the value obtained in the analysis of the CIV absorptions represented in Table 2. This agreement suggests that our crude opaque-translucent models give a reasonably accurate representation of the details of the absorption profile in Fig. 6.

The two component models gave us a freedom to explore a range of h values much larger than $1R_*$. This became apparent in our trials for models similar to those shown in Fig. 6, with $r_o \geq 10R_*$. As shown in the figure, h values as small as $\frac{1}{4}R_*$ blur the “M minimum” at $\phi \approx 0.00$ to invisibility. We were able to fit the data with (opaque component) h values in the broad range of $\frac{1}{4}–1R_*$.

5.3. Fitting of $H\alpha$ variations with phase

The $T_{disk} = 7,500$ K and column density for the cool disk component determined from the iron lines is sufficient to

make the optical depth in $H\alpha \sim 5$, thereby satisfying one of the assumptions of our occultation models.

In contrast to the UV resonance lines, it is relatively easy to fit $H\alpha$ absorption data even with our opaque component disk. In Figure 7 we exhibit the $H\alpha$ absorption profiles for the two occultations of the rotation cycle. To match the zero point of the equivalent width data to the models, we subtracted a plateau level of the equivalent width average, 1.34 \AA at nonoccultation phases and scaled the peak absorption value to 1.0 (all flux removed by the disk) for comparison with the models. Because the data on either side of the maxima seems to follow a common relation, we reflected the data around the centroid phase ($\phi = 0.00$ and 0.55 phases).

Before proceeding to the modeling analysis, we digress to discuss two important attributes of the $H\alpha$ curves that demonstrate that the assumption of *planarity* of our geometrical disk models cannot be quite right:

- Fig. 7a exhibits a plateau near $\phi = 1.00$. This plateau is more apparent for the dots, which are flat for phases 0.98–1.00. The squares (**post-occultation data**) beyond 0.01 fall off more rapidly from the peak at 0.0 than the dots (**pre-occultation data**). This fact hints at a difference in h on either side of the central plane and may manifest a slight warping of the disk.
- A faint but distinct absorption may be present at phases separated from the central lobe maxima; see the feature in the phase range $\phi = 0.86–0.93$. A similar out-of-plane absorption is evident at Fig. 7b at $\phi = 0.40–0.48$. These features can be interpreted as matter **separated from** the disk torus. As an alternative to the planar disk geometry, Michel & Sturrock (1974), Nakajima (1985), Preuss et al. (2004), and TO05 have suggested that the wind particles will collect in local equipotential regions. **The locus of this surface depends upon** the balance of magnetic, radiative, and may have relevance to these features.

As in the CIV analysis, the h value drives the shape of the central core absorption near $\phi = 1.00$. Likewise, the half-width and the slopes of the profile are sensitive to the r_i and r_o radii, respectively. For small disk models, we could achieve matches only with thin rings, that is $r_o \approx r_i$. However, for values of r_o below $8 R_*$, we had difficulty fitting even thin rings to the data. For models with $r_o \geq 10R_*$ the fitting was easy, and the ratio of inner to outer radii quickly settled to about 30% in Fig. 7a. The **dot-dashed** line in this panel (just visible **between** $0.90 \leq \phi \leq 0.95$) gives a best fit for the opaque-component (only) family with $r_o = 10R_*$. For larger r_o values, r_i approximately scales with the same semiheight. Our geometric models by themselves do not allow us to rule out larger disks.

To examine the influence of a thin (in direction perpendicular to the plane) disk, we have also computed a sample “M-shaped” core in Fig. 7a for a model with a semiheight $h = \frac{1}{3}R_*$. This model is represented by the dot-dashed line.

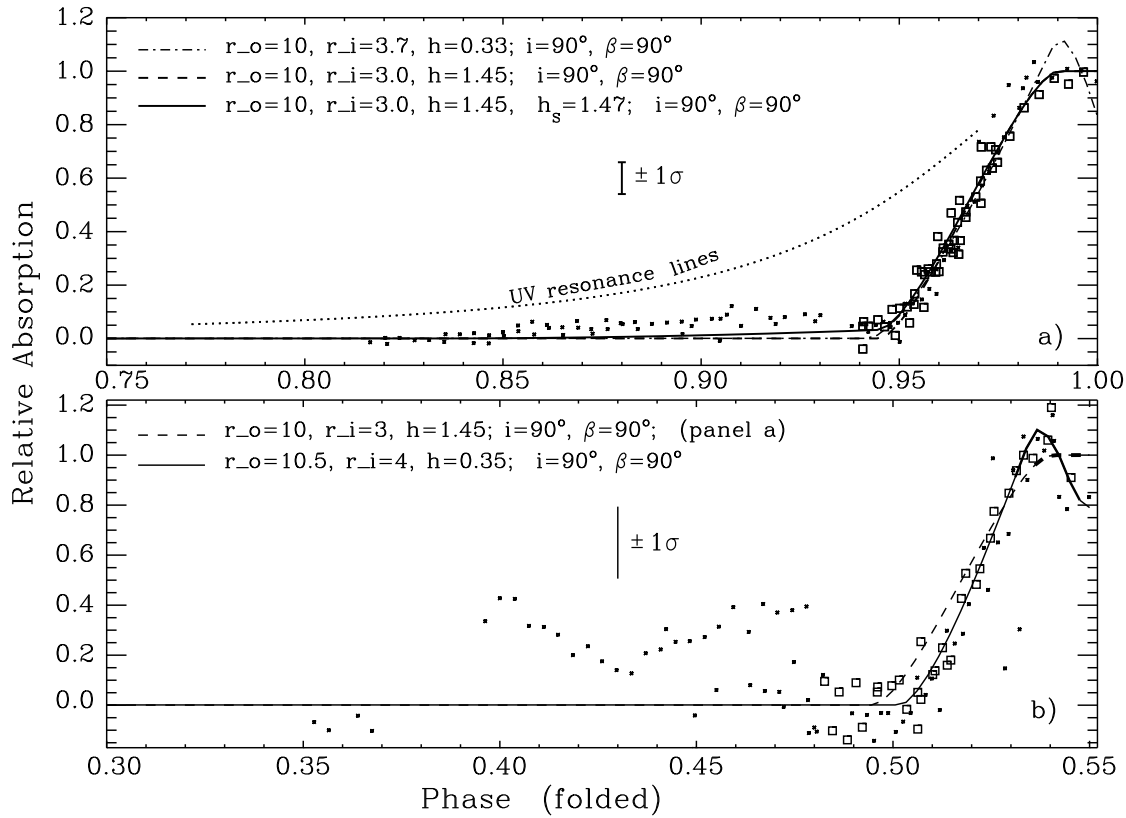


Fig. 7. *Panel a:* Fits to excess H α absorption with phase for the primary occultation of 36 Lyn centered at $\phi = 1.0$, similar to Fig. 6 for CIV. Coded lines are fits for indicated disk dimensions computed from one-component (dashed) and two-component (solid) disk-absorption models. Dots and squares represent observations made before and after mid-occultation, respectively. Mean 1σ error bars refer to the 2σ taken from Paper 1. *Panel b:* Fits to H α data responsible for the secondary occultation centered near $\phi = 0.55$. The best fit model from panel *a*, with semiheight $h = 1.45R_*$, is shown to be too thick for this disk sector. The scaling is normalized to unity for the maximum absorption and thus is enlarged relative to the scale of *panel a*.

This attempt clearly does not fit the data for the primary occultation. Indeed, the best semiheight we found was $h = 1.45R_*$, which is probably within the errors of the h value determined from CIV absorptions. The secondary occultation event represented in Fig. 7b tells a different story. First, the absolute maximum of this absorption curve is only 33% as strong as the absorption in the primary occultation. Consequently, the effects of noise are much larger. Nonetheless, inspection shows that this maximum has almost exactly the same half-width and fall-off gradient with phase as the primary. One difference with respect to the primary maximum is that the H α absorption curve exhibits a possible M-shape, reaching down some 25% from the maximum height at $\phi \approx 0.538$. The significance of this inference is drawn from five observations in this diagram, of which four are much lower than unity by more than the error bars. In Fig. 7b we show both our best fit for the primary maximum occultation in Fig. 7a (dashed line) and the best fit for the secondary maximum, this time with a semiheight $h = 0.35R_*$. The best r_o and r_i values for both occultations are practically the same. According

to this result, the two opposite sectors are similar, with the important difference that the sector responsible for the secondary occultation is four times thinner in height.

How does our finding that H α is formed closer to the plane than CIV fit into our current understanding of the disk dynamics? In the Donati et al. (2002) and uO02 models, newly shocked wind particles cool and settle into a thin disk. The H α -absorbing volume can be expected to overlap the cool component we identified from our Fe line analysis. Our standard model of the cool component predicts an excess H α absorption, for full-disk occultation, of 0.18Å. This value happens to be the same as the peak excess absorption given in Paper 1. This agreement is fortuitous, considering that we have compared moderately optically thick H α and optically thin Fe II lines in (probably) only partially overlapping volumes.

6. Conclusions

We can recap the conclusions of this paper as follows:

1. Like the circumstellar disks of early-type Bp stars, the static “disk” of 36 Lyn consists of both a cool and a hot component. In general terms, this confirms the hydrodynamic result of Babel & Montmerle (1997) for IQ Aur. The cool component of 36 Lyn is observed in the Fe-group lines (mainly Fe^{2+}) arising from low excitation states; the hot component is visible in the UV resonance lines. The volume in which $\text{H}\alpha$ absorption is formed probably overlaps both these regions, but we do not know the extent of this overlap.
2. We have determined the temperature of the cool disk component to be $7,500 \pm 500 \text{ K}$ from an analysis of Fe II and Fe III lines variations during primary disk occultation. The temperature ratio $T_{\text{disk}}/T_{\text{eff}} \approx 0.6$ for 36 Lyn. This is also the ratio SG01 found for the hot Bp stars σ Ori E and β Cep.
3. The physical parameters of this disk, including its column density, insure that the strongest low-excitation lines are readily visible in IUE spectra, but they are not quite sufficient to allow the disk component to be visible in even strong optical Fe lines.
4. The ionization temperature(s) determined from the presence of disk NV and CIV absorptions reveal that part of the disk is heated, perhaps to $30,000 \text{ K}$ or more. For CIV there is only a hint of emission at non-occultation phases, unlike the disks of hotter Bp stars.
5. The relative heights of the absorption maxima corresponding to the occultations by two disk segments differ among the highly excited “super ions” (NV, CIV, and SiIV) themselves and with respect to resonance lines of less excited ions. The two opposing disk segments do not exhibit the same ranges of ionization. The disk sector responsible for absorptions at $\phi = 0.00$ has a more restricted temperature range than the sector visible at $\phi \approx 0.55$. The existence of restricted temperatures implies that the production of the “super ions” does not result from the irradiation of gas by local soft X-rays.
6. Geometric modeling of the occultation from the UV resonance and $\text{H}\alpha$ lines suggests that the inner edge of the disk (ring) is detached from the star’s surface. The inner edge is located at $\approx \frac{1}{3}r_o$. This conclusion is secure for $\text{H}\alpha$ but is less secure for the UV data.
7. Analysis of the equivalent width maxima of the $\text{H}\alpha$ shows clearly that the associated opposing disk sectors have nearly the same inner and outer disk values. They differ by a factor of 3 in their heights above the magnetic plane. The secondary absorption appears to be weaker because the disk sector responsible for it is thinner (measured out of the disk plane) than the opposing segment by about the same factor.
8. Like $\text{H}\alpha$, the UV resonance lines are opaque near the central plane. Their absorptions are formed in volumes having nearly the same range of radii as the $\text{H}\alpha$ absorption (i.e., from $3R_*$ to $10R_*$). The UV resonance lines indicate significant additional translucent extensions beyond this height, with $h_S/h \approx 3$.

Acknowledgements. This work was supported in part by NASA grant NNG04GE75E. The optical data were obtained using the MuSiCoS spectropolarimeter at Pic Du Midi Observatory, the Canada-France-Hawaii Telescope, operated by the National Research Council of Canada, the Centre National de la Recherche Scientifique of France, the University of Hawaii, the Dominion Astrophysical Observatory, Herzberg Institute of Astrophysics, and the David Dunlap Observatory, University of Toronto. C. T. Bolton’s research was partially supported by a Discovery Grant from the Natural Sciences and Engineering Research Council of Canada. John Liska and Mel Blake assisted in obtaining and reducing the DDO spectra.

References

Babel, J. 1997, A & A, 309, 867
 Babel, J. & Montmerle, T. 1997, A&A, 323, 121 (BM97)
 Babel, J. & North, P. 1997, A & A, 325, 195
 Bjorkman, K., S., Bjorkman, J. B., & Wood, 2000, in The Be Phenomenon in Early-Type Stars, ed. M. Smith, H. Henrichs, & J. Fabregat, ASP Conf. Ser. 214, 603.
 Donati, J-F., Babel, J. et al. 2002, MNRAS, 333, 55
 Floquet, M., Neiner, C. et al. 2002, A. & A., 394, 137
 Henrichs, H. F., de Jong, J. A. et al. 1998, Ultraviolet Astrophysics Beyond the IUE Final Archive, ed. R. Harris, ESA SP-413, (Noordwijk: ESA), 157
 Hubeny, I. 1996. & Heap, S. R. 1996, ApJ, 470 1144
 Hubeny, I. & Lanz, T., 1996, priv. comm.
 Hubeny, I., Lanz, T., & Jeffery, C. S. 1994, Newslett. Anal. Astron. Spectra, 20, 30
 Kurucz, R. L. 1993, ATLAS9 Stellar Atmospheres and 2 km s^{-1} Grids, Kurucz CD-ROM #13
 Levay, K. 2003, priv. commun.
 MacFarlane, J. J., Cohen, D. H., Wang, P. 1994, ApJ, 437, 351
 Michel, F. C., & Sturrock, P. A. 1974, Planet. Space Sci., 22, 1501
 Nakajima, R. 1985, Ap. & S. S., 116, 285
 Neiner, C., Henrichs, H. F. et al. 2003, A & A, 411, 565
 Preuss, O., Schüssler, M. et al. 2004, A & A, 417, 987
 Shore, S. A., 1987, AJ, 94, 731
 Shore, S. A., & Brown, D. N. et al. 1990, ApJ, 348, 242 (SB90)
 Shore, S. A., & Brown, D. N. 1990, ApJ, 365, 665
 Shore, S. A., Bohlender, D. A. et al. 2004, A. & A., 421, 203
 Smith, M. A. 2001, ApJ, 562, 998
 Smith, M. A. & Groote, D. 2001, A. & A., 372, 208 (SG01)
 Smith, M. A., Sterken, C. & Fullerton, A. W. 2005, ApJ, 564, 1300
 Stahl, O., Kaufer, A., et al. 1996, A. & A., 312, 539
 Tonneon, S., K., Cohen, D. H. et al. 2002, BAAS, 201, #113.01
 Townsend, R. H. D. & Owocki, S. P. 2005, MNRAS, 357, 251 (TO05)
 ud-Doula, A., & Owocki, S. P. 2002, ApJ, 576, 413 (uO02)
 Wade, G. A., Smith, M. A. et al. 2006, A&A, xxx, yyy (Paper 1)
 Walborn, N. R., & Nichols, J. S. 1994, ApJ, 425, L29